JACS
JOURNAL OF THE AMERICAN CHEMICAL SOCIETY
pubs.acs.org/JACS
Article

Photocatalytic Ammonia Synthesis using Fe-Based MOFs: The Role of Ligand Functionalization

Jana Bischoff, Cornelia von Baeckmann,* Shaghayegh Naghdi, Adrian Ertl, Vasily Vorobyev, Anastasiia Naryshkina, Lakhanlal, Hanspeter Kählig, Laura Kronlachner, Robert T. Woodward, Freddy Kleitz, Andreas Limbeck, Maytal Caspary Toroker, Amanda J. Morris, and Dominik Eder*

Cite This: J. Am. Chem. Soc. 2026, 148, 21382−21392
Read Online

ABSTRACT: Photocatalytic ammonia (NH_3) synthesis offers a carbon-neutral alternative to the Haber−Bosch process, which generates 42 million metric tons of CO_2 equivalent emissions annually. However, solar-to-ammonia conversion with contemporary photocatalysts remains far from practical requirements, and understanding the limiting factors in systems with well-defined active sites is crucial. Here, we show how the μ_3-oxo-centered trinuclear Fe cluster in MIL-101(Fe) functions as the catalytic motif for N_2-to-NH_3 conversion through combined experimental and computational investigations. Comparative studies with a molecular analogue demonstrate that the cluster is stabilized within the MOF framework, sustaining redox cycling and maintaining high catalytic activity. We systematically functionalized the dicarboxylate ligands of MIL-101(Fe) with $-NH_2$, $-Br$, $-NO_2$, $-F$, and $-CF_3$ to probe how ligand chemistry modulates Fe electron density, N_2 adsorption capacity, and proton availability, correlating these properties with catalytic performance using spectroscopic and surface characterization techniques alongside time-resolved infrared to assess excited-state lifetimes. F-functionalization optimally balances N_2 activation, proton availability at Fe active sites, and excited-state lifetimes, boosting NH_3 production by ∼ 60% relative to unmodified MIL-101(Fe). This study of ligand-functionalized MIL-101(Fe) MOFs uncovers the underlying structure-activity relationships and advances design principles for solar-driven NH_3 synthesis.

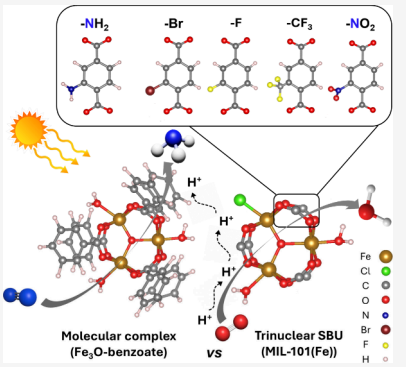

INTRODUCTION

Ammonia (NH_3) is an essential feedstock in the chemical industry with critical applications in the production of fertilizers, pharmaceuticals, and numerous other nitrogen-containing compounds.[1] Its potential as a carbon-free hydrogen carrier, with a high hydrogen content, further underscores its importance in sustainable energy solutions.[2,3] The Haber-Bosch process has enabled large-scale NH_3 production for over a century but remains highly energy-intensive and dependent on fossil-fuel-derived hydrogen, making it one of the most carbon-intensive industrial processes.[4,5] Photocatalytic NH_3 synthesis is envisioned as a promising alternative, requiring only solar energy, nitrogen, and water as a proton source, thereby eliminating the need for external energy input.[6] However, the activation of the inert N≡N bond[7] without external energy assistance presents a significant challenge for the catalyst. Additionally, coupling water oxidation to provide protons and N_2 reduction in a single system, along with the associated multielectron hydrogenation pathway[7] limit the solar-to-ammonia conversion efficiency.

Metal−organic frameworks (MOFs), as porous materials with well-defined active sites, composed of metal-oxo clusters (secondary building units, SBUs) and organic ligands, have gained increasing interest as catalysts for solar-driven NH_3 synthesis.[8] Owing to their modular architecture, MOFs present a tunable well-defined platform to investigate fundamental aspects such as performance limiting factors in photocatalysis. Recently, the use of various metal nodes and fine-tuning of electron density via ligand functionalization to modulate catalytic activity has attracted significant interest.[9−11] Among the various metal centers explored, Fe stands out due to its biological relevance in nitrogenase, where half-filled d orbitals facilitate N_2 activation under ambient conditions.[12,13] Notably, frameworks featuring trinuclear μ_3-oxo-bridged SBUs (such as MIL-100, MIL-101, and MIL-88B) outperform mononuclear representatives like MIL-53[14,15] and MIL-68,[16] highlighting the superiority of trinuclear oxo-bridged SBU for efficient NH_3 synthesis. Several strategies have been explored to improve the photocatalytic performance of MIL-101(Fe), including defect engineering to increase the accessibility of Fe sites,[14] creation of mixed-valence Fe(II)/Fe(III) SBUs,[17] enhancement of

Received: December 19, 2025
Revised: April 27, 2026
Accepted: April 28, 2026
Published: May 19, 2026

https://doi.org/10.1021/jacs.5c22833
J. Am. Chem. Soc. 2026, 148, 21382−21392

charge separation via metal doping[18] as well as incorporation of secondary metals in mixed-metal x/Fe SBUs.[19,20] Our strategy entails rational modification of organic ligands by introducing substituents that vary in steric demand and electronic character, ranging from electron-donating to strongly electron-withdrawing groups with distinct inductive and resonance effects. This approach enables us to disentangle the multiple effects imposed by ligand functionalization, elucidating how each factor influences photocatalytic performance. As such, our study provides crucial mechanistic insight into this emerging photocatalytic application (Figure 1).

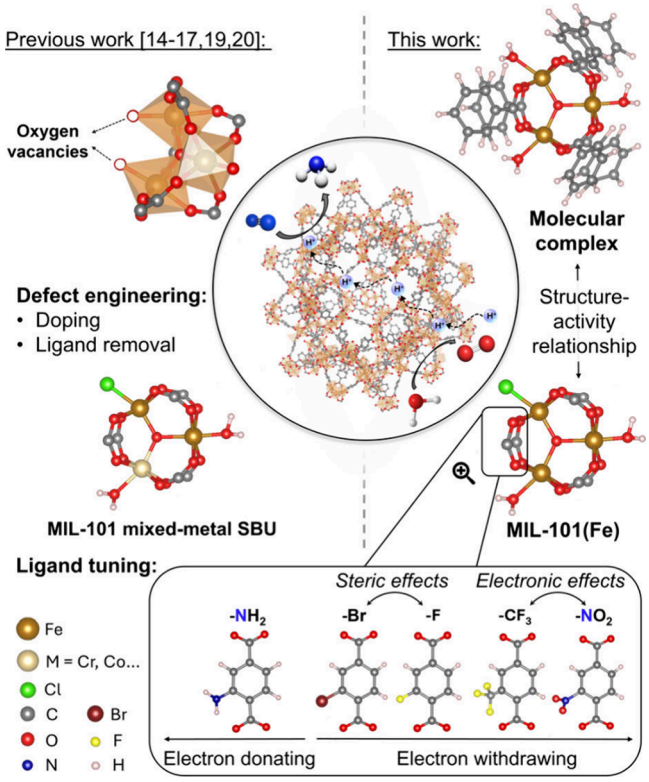

Figure 1. Schematic representation of the present study, illustrating ligand functionalization as a strategy to tune the electronic and steric environment of the MOF SBU.

RESULTS AND DISCUSSION

Materials Characterization

MIL-101(Fe) and the μ-oxo-centered trinuclear iron carboxylate complex $[Fe_3O(PhCOO)_6(H_2O)_3]ClO_4$ (hereafter referred to as the Fe_3O-Bz complex) were synthesized following published procedures (details in Methods).[21,22] Powder X-ray diffraction (PXRD) confirmed the expected crystalline structures of MIL-101(Fe) without secondary phases or impurities (Figure S1). Scanning electron microscopy (SEM) revealed octahedral MOF particles ranging from several hundred nanometers to the micrometer scale (Figure 2c). Thermogravimetric analysis (TGA) showed structural integrity up to 300 °C, in contrast to the molecular analogue, which undergoes degradation at 165 °C (Figures S3a-S4). Fourier-transform infrared (FTIR) spectroscopy further verified the composition of both MIL-101(Fe) and the molecular analogue, showing characteristic bidentate bridging coordination, as evidenced by asymmetric and symmetric $\nu_{as}(COO^-)$ and $\nu_{sym}(COO^-)$ modes at 1591 and 1384 cm^{-1}, respectively, for MIL-101(Fe), with slightly shifted positions observed in the molecular analogue (Figure 2b). X-ray photoelectron spectroscopy (XPS) was employed to probe the surface electronic states (Figures S6a and S7a). The Fe 2p spectrum of MIL-101(Fe) displays binding energies at 710.2 eV (Fe $2p_{3/2}$) and 723.3 eV (Fe $2p_{1/2}$), characteristic of high-spin Fe^{3+} accompanied by satellite shakeup features.[23] Similar Fe 2p binding energies are observed for the molecular analogue, with slight shifts to higher values (Figures S6g and S7g), attributed to difference in terminal ligands. In the molecular analogue, three aqua ligands coordinate to the $Fe_3(\mu_3$-O) core, resulting in a cationic complex, whereas in MIL-101(Fe), replacement of one aqua ligand by a chloride provides overall charge balance. Nitrogen physisorption analysis at 77 K of MIL-101(Fe) revealed characteristic Type I isotherms with secondary uptakes at $p/p_0 \approx 0.1$ and $p/p_0 \approx 0.2$, consistent with the presence of two types of microporous windows characteristic of the multiscale porosity of MIL-101(Fe) (Figure S8a). The corresponding NLDFT pore size distribution shows four distinct pore sizes centered at ~ 0.6 nm, ~ 1.1 nm, and ~ 2.1 nm with an additional shoulder at ~ 2.7 nm (Figure S8b). These features can be assigned to the internal cavity of the structural supertetrahedron (ST) enclosed by four SBUs, a smaller cage with a pentagonal window, and a larger asymmetric cage with a hexagonal window (structural motifs shown in Figure S10). The apparent Brunauer–Emmett–Teller (BET) surface area was calculated as 2845 $m^2\ g^{-1}$, in good agreement with previous reports.[24,25] UV–vis diffuse reflectance spectra (DRS) of the Fe_3O–Bz complex and MIL-101(Fe) display an intense absorption band centered at ~ 410 nm, assigned to ligand-to-metal charge transfer (LMCT), together with a weaker absorption feature at longer wavelengths and a broad absorption edge extending to ~ 600 nm.[26−29] These features confirm that both the molecular complex and the extended MOF framework exhibit comparable optical responses (Figure S11).

Next, a series of isostructural mixed-ligand MIL-101(Fe)-based MOFs was synthesized with varying ratios of terephthalic acid (BDC) to amino-terephthalic acid (NH_2–BDC), denoted as xNH_2-MIL-101(Fe), where x represents the percentage of NH_2–BDC ligand. All compositions were obtained via solvothermal method (details provided in the Methods). The expected MIL-101(Fe) framework structure was confirmed for all samples by PXRD, SEM, and XPS (Figures S1b; S2, panels f–i; and S6–S7, panels h–k). The actual ligand composition in the mixed-ligand MOFs was quantified by digesting the powders using a 1 M NaOH solution followed by recrystallization with deuterium chloride (DCl) and ^{1}H NMR spectroscopy (Figure S14 and Table S1).

Formation of mixed-ligand phases is further supported by FTIR spectra of xNH_2-MIL-101(Fe) samples (x = 2%, 5%, 17%, 29%) and the single-ligand NH_2-MIL-101(Fe), which exhibit characteristic asymmetric and symmetric N–H stretching bands at 3465 and 3325 cm^{-1}. These bands increase in intensity proportionally with the NH_2–BDC content, accompanied by the appearance of a C–N vibration at 1252 cm^{-1} (Figure S5a), typical of aromatic amines. Notably, a gradual redshift of the $\nu_{as}(COO^-)$ peak was observed with increasing NH_2–BDC ligand content, indicating a weakening of the coordination bond strength (Figure S5b). This shift can be attributed to two factors: (i) the resonance effect of the NH_2 group with the π system, which increases electron density

https://doi.org/10.1021/jacs.5c22833
J. Am. Chem. Soc. 2026, 148, 21382−21392

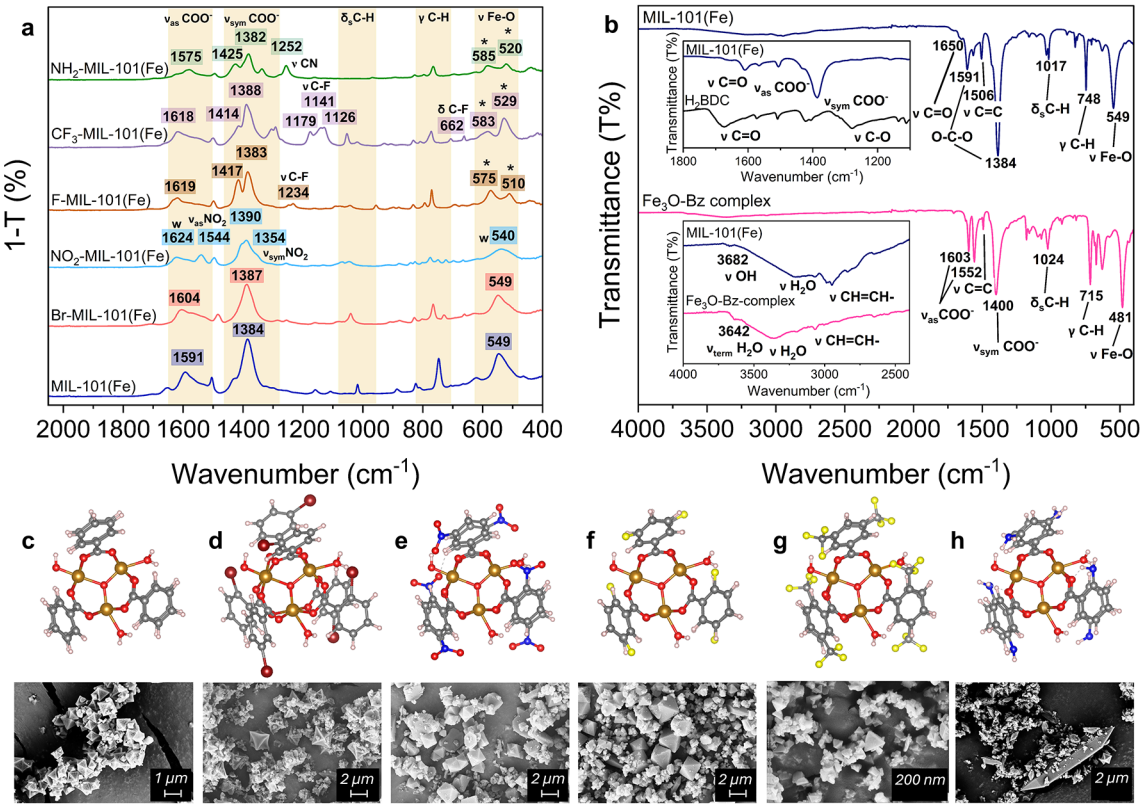

Figure 2. Characterization of single-ligand MIL-101(Fe) derivatives: (a) FTIR spectra of MIL-101(Fe) derivatives incorporating BDC, NO_2−BDC, Br-BDC, F-BDC, NH_2−BDC, and CF_3−BDC ligands, showing ligand-specific vibrational features. Hybridization of the NO_2 group with the aromatic ring broadens the $\nu_{as}(COO^-)$ and ν(Fe−O) bands in NO_2-MIL-101(Fe), indicated as wide (w). (b) FTIR spectra of as-prepared MIL-101(Fe), with an inset comparing the spectrum of the H_2BDC ligand, and Fe_3O-Bz complex compared to MIL-101(Fe), with an enlarged view of the OH and aromatic C−H stretching regions. (c−h) SEM images of the as-prepared MOF samples: (c) MIL-101(Fe), (d) Br-MIL-101(Fe), (e) NO_2-MIL-101(Fe), (f) F-MIL-101(Fe), (g) CF_3-MIL-101(Fe), and (h) NH_2-MIL-101(Fe).

and reduces carboxylate electrophilicity, thereby diminishing its ionic character toward Fe^{3+} according to the HSAB principle[37] and (ii) intraframework N−H···O hydrogen bonding between the NH_2 group and one of the four carboxylate O atoms, which lowers its effective negative charge. Further changes in the coordination environment are evident in the Fe−O stretching region. While non−modified MIL-101(Fe) shows a band at 549 cm^{-1}, the mixed−ligand MOFs display a shoulder at 585 cm^{-1} whose intensity increases with NH_2−BDC content. This feature supports the presence of asymmetric coordination modes influenced by N−H···O hydrogen bonding. Finally, TGA analysis revealed decomposition temperatures between 270 and 325 °C (Figure S3b), with the onset temperature decreasing progressively with higher NH_2−BDC content, in line with the FTIR-indicated weakening of the coordination strength. Nitrogen physisorption isotherms for all ligand ratios showed the expected decrease in surface area with increasing NH_2−BDC content (Figure S8, panels m-n; Table S2). In addition to these structural changes, the amine functional group in the organic ligand acts as a chromophore,[30,31] leading to bandgap narrowing as observed in DRS measurements (Figure S12).

To exclude effects arising from different ligand ratios, single-ligand, monosubstituted MIL-101(Fe) variants were synthesized, including NO_2-, Br-, and NH_2-MIL-101(Fe), as well as, to our knowledge, the novel F- and CF_3-MIL-101(Fe). The expected framework structure of all variants was confirmed by PXRD, SEM, and XPS analyses (Figures S1a; Figure 2, panels c-h; and Figures S6−S7, panels b-f). PXRD patterns show minor differences in relative peak intensities among functionalized MIL-101(Fe) derivatives, most notably for CF_3-MIL-101(Fe), consistent with slightly smaller particle sizes observed in SEM images (Figure 2g).

The impact of electron-withdrawing groups (EWGs) − Br, NO_2, F and CF_3 − on Fe-ligand coordination is reflected in the FTIR spectra of NO_2-, Br-, F-, and CF_3-MIL-101(Fe) (Figure 2a). A blueshift of the $\nu_{as}(COO^-)$ peak is observed in all four EWG-MOFs compared to nonfunctionalized MIL-101(Fe), indicating increased C−O bond polarization and a corresponding strengthening of the coordination bond. The same factors that modulate coordination strength in amine-functionalized MOFs must also be considered here: (i) electron withdrawal through the ligand's π system and (ii) direct interaction between the functional group and the carboxylate O atom. In the case of EWGs, this direct interaction is expected to be repulsive, due to electrostatic repulsion between the substituent (e.g., F, Br, NO_2, or CF_3) and the carboxylate O atoms. In F-MIL-101(Fe) and CF_3-MIL-101(Fe), the $\nu_{sym}(COO^-)$ stretch splits into two bands at 1383 and 1417 cm^{-1} for F-MIL-101(Fe), and 1388 and 1414 cm^{-1} for CF_3-MIL-101(Fe), with the splitting more distinct in F-MIL-101(Fe). The Fe−O bands are observed at 575 and 510 cm^{-1} for F-MIL-101(Fe) and 583 and 529 cm^{-1} for CF_3-MIL-101(Fe), with the larger Fe−O separation in F-MIL-101(Fe). The enhanced $\nu_{sym}(COO^-)$ splitting and greater Fe−O band separation in F-MIL-101(Fe) indicate a more direct interaction

https://doi.org/10.1021/jacs.5c22833
J. Am. Chem. Soc. 2026, 148, 21382−21392

between the fluorine substituent and the carboxylate O atoms, whereas the CF_3 group, being more spatially distant, this effect is weaker. Br-MIL-101(Fe) does not show pronounced asymmetric features, likely due to weaker repulsion between Br and the carboxylate oxygens. For NO_2-MIL-101(Fe), the coordination bands appear broader, reflecting resonance interactions with the BDC π system that enhance electronic delocalization. The $\nu_{as}(COO^-)$ band shows the largest blueshift in NO_2-MIL-101(Fe), whereas F- and CF_3-MIL-101(Fe) exhibit intermediate shifts due to inductive effects, and Br-MIL-101(Fe), with a weaker inductive character, shows the smallest shift.

To further confirm that ligand functionalization does not distort the Fe_3O cluster, DFT calculations on the SBU were performed. These results show that interactions between the functional groups (F, CF_3, NH_2) and the carboxylate oxygen atoms do not induce significant structural changes. The Fe−O coordination bond lengths and Fe−O−Fe angles, as well as the central O−Fe distances, remain essentially unchanged across all functionalized MOFs, even for the bulkiest CF_3 variant (Figures S41−S42; Tables S13−S14). Thus, while the IR spectra reflect local polarization and electronic effects, the overall geometry of the Fe_3O cluster is preserved, in agreement with previous computational studies.[32]

TGA analysis of the single-ligand MIL-101(Fe)-based MOFs (Figure S3a) shows decomposition temperatures of 262 °C for Br-MIL-101(Fe), 314 °C for NO_2-MIL-101(Fe), 329 °C for F-MIL-101(Fe), and 339 °C for CF_3-MIL-101(Fe). Nitrogen adsorption isotherms revealed Type I behavior for all samples (Figure S8), indicating that the characteristic topology of MIL-101(Fe) is retained despite ligand functionalization. Pore size distributions reflect the steric influence of the ligands. The smallest pores (∼ 0.61 nm) are only subtly affected, whereas the differential pore volumes of larger cages (1.1, 2.1, and 2.7 nm) decrease with increasing ligand bulk, with the corresponding PSD peaks appearing broader and less resolved, specifically for CF_3-MIL-101(Fe). The resulting trend in specific surface areas is MIL-101(Fe) > F-MIL-101(Fe) > NH_2-MIL-101(Fe) > Br-MIL-101(Fe) > NO_2-MIL-101(Fe) > CF_3-MIL-101(Fe), with a similar pattern observed for total pore volumes (Table S2). While ligand substitution modulates pore volumes and surface areas, the intrinsic porosity and framework architecture is maintained. DRS and Tauc plots of monofunctionalized MIL-101(Fe) variants revealed similar absorption edges across all samples (Figure S13). Consistent with FTIR observations, Br- and F-substituted samples show only minor band gap changes, reflecting the modest influence of their electron-withdrawing (−I) inductive effects. For CF_3-MIL-101(Fe), the effect is even less pronounced: although CF_3 is strongly electron-withdrawing, it primarily exerts a through-bond inductive effect without significant conjugation with the aromatic BDC π system, resulting in minimal modulation of the MOF's band gap.[33] In contrast, NO_2−BDC induces a more pronounced band gap reduction of approximately 0.3 eV compared to nonfunctionalized MIL-101(Fe), arising from conjugation between the NO_2 group and the BDC π-system, with NO_2, acting as an electron acceptor, facilitating electron withdrawal from the aromatic carbon.[33]

To assess the transferability of the ligand functionalization strategy across related frameworks, MIL-88B(Fe), which shares the same Fe_3-μ_3-oxo SBU, and its F-functionalized analogue were synthesized and characterized. PXRD, SEM, and XPS confirmed the expected structure (Figures S1d, S2h,i, S6, and S7l,m). While pristine MIL-88-type materials typically exhibit negligible BET surface area due to a closed-pore structure, ligand functionalization can suppress this contraction, resulting in increased accessible pore size and surface area.[34,35] This effect is evident as well in our samples, where MIL-88B(Fe) exhibits a low surface area of 564 $m^2\ g^{-1}$, which increases significantly to 1510 $m^2\ g^{-1}$ for F-MIL-88B(Fe). Both N_2 physisorption isotherms correspond to Type I (Figure S9), with the F-functionalized variant showing higher uptake at very low p/p_0, typical of micropore filling, and consequently a higher micropore area (Table S2). FTIR analysis reflects trends similar to those observed for the MIL-101(Fe) structure. In the fluorine-functionalized MOF, characteristic band splitting of the $\nu_{sym}(COO^-)$ and Fe−O modes is observed (Figure S5c). TGA reveals that MIL-88B(Fe) has comparable thermal stability to MIL-101(Fe), with a degradation onset at 333 °C. The F-functionalized MIL-88B(Fe) exhibits slightly lower thermal stability, with an onset at 318 °C (Figure S3c). DRS spectra (Figure S14c) reveal the same electronic transitions for both MIL-88B(Fe) variants, as for MIL-101(Fe) (∼ 410 nm and ∼ 470 nm), consistent with literature reports.[36,37] The F-functionalized variant exhibits higher absorbance, which reduces the optical bandgap, as shown in the corresponding Tauc plots (Figure S14d).

Photocatalytic Activity

The photocatalytic NH_3 synthesis activity of MIL-101(Fe) and its functionalized derivatives was evaluated in N_2-saturated ultrapure water under continuous visible light irradiation (AM 1.5 G, $\lambda \geq 420$ nm, 23 mW cm^{-2}) using a 150 W xenon arc lamp. Reactions were carried out in a custom-made quartz reactor equipped with a circulating water jacket to maintain a constant temperature of 15 °C (Figure S15). Prior to the reaction, catalysts were activated at 120 °C under vacuum for 12 h to remove adsorbed gases, particularly nitrogen, which could otherwise lead to false positives. The reaction mixture consisted of 5 mg of catalyst dispersed in HPLC-grade water, which was purged with argon to eliminate contamination from external nitrogen sources. To ensure that the NH_3 originated from N_2-to-NH_3 conversion and not from labile nitrogen-containing compounds typically found in the N_2 gas stream,[38] the atmosphere, or the catalyst itself, control experiments were performed: (i) without the catalyst, (ii) without light irradiation, and (iii) without N_2 input. These control experiments ruled out contributions from external sources and confirmed the detection accuracy (Table S3).

The NH_4^+ concentrations, as a proxy for NH_3 synthesis, in the liquid phase were quantified using the Nessler's reagent colorimetric method (Figure S16) and qualitatively confirmed via ^1H NMR spectroscopy of the reaction supernatant (Figure S17). We observed a decrease in NH_4^+ production yield with increasing NH_2−BDC content (Figure 3a). All samples were tested for hydrogen evolution (HER) using gas chromatography, and for hydrazine (N_2H_4), nitrate (NO_3^-), and nitrite (NO_2^-) formation by UV−vis spectrometry to assess selectivity. No side products or N_2H_4 intermediates were detected in any case (Figures S18−S20, Table S4). While previous studies have associated amino functionalization with enhanced photocatalytic activity due to increased light absorption,[3940,41] our results reveal the opposite trend - despite a gradual bandgap reduction confirmed by Tauc plots (Figure S12b), consistent with observations in NH_2-MIL-125(Ti).[42] We hypothesize that in NH_2-MIL-101(Fe), photo-

https://doi.org/10.1021/jacs.5c22833
J. Am. Chem. Soc. 2026, 148, 21382−21392

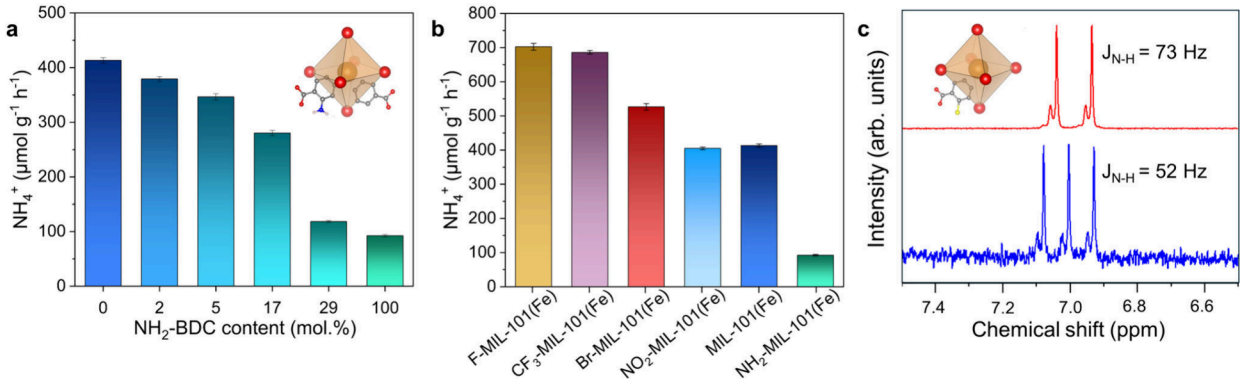

Figure 3. Photocatalytic NH_4^+ production rates for (a) mixed-ligand xNH_2-MIL-101(Fe) MOFs and (b) single-ligand monofunctionalized MIL-101(Fe) variants (F-, CF_3-, Br-, NO_2-, NH_2-, and unmodified MIL-101(Fe)). Error bars represent standard deviation from triplicate measurements. (c) ^{1}H NMR spectra of solution after 1 h photocatalysis using F-MIL-101(Fe) in $^{14}N_2$ and $^{15}N_2$ atmosphere.

excitation-induced LMCT may cause holes to accumulate at the NH_2 nitrogen, which inhibits water oxidation and reduces the availability of protons, thereby slowing NH_4^+ formation. This interpretation is supported by projected density of states (PDOS) analysis, which shows that the states just below the Fermi level in the amino-functionalized MOF originate predominantly from the nitrogen atom (Figure S26e). This suggests that these orbitals are where holes tend to localize after photoexcitation. Our hypothesis is supported by linear sweep voltammetry (LSV) under visible-light irradiation (AM 1.5 G, $\lambda \geq 420$ nm, 23 mW cm^{-2}, 150 W Xe lamp), which shows that NH_2-MIL-101(Fe) exhibits a positive anodic onset and reduced photocurrent compared to pristine MIL-101(Fe) (Figures S21 and S22). This observation is consistent with transient photocurrent measurements under chopped light, where the NH_2-functionalized MOF generates lower photocurrents.

While these results provide a clear trend, additional factors related to ligand functionalization should be considered, including changes in Fe Lewis acidity (influencing N_2 activation), variations in excited-state lifetime, and functionalization-induced changes in pore structure that affect reactant accessibility as well as proton transfer due to altered surface charge.

To investigate the influence of EWGs, we compared the photocatalytic NH_4^+ synthesis performance of single-ligand MIL-101(Fe) variants. NO_2-MIL-101(Fe) (404 μmol g^{-1} h^{-1}) exhibited activity nearly identical to unmodified MIL-101(Fe) (413 μmol g^{-1} h^{-1}), whereas Br-MIL-101(Fe) showed a substantial increase (526 μmol g^{-1} h^{-1}). The highest activity was observed for F-MIL-101(Fe), which generated 702 μmol g^{-1} h^{-1}, closely followed by CF_3-MIL-101(Fe) at 686 μmol g^{-1} h^{-1} (Figure 3b). Isotope-labeling experiments using F-MIL-101(Fe) confirmed that NH_4^+ originates from introduced N_2. Experiments under $^{14}N_2$ atmosphere, ^{1}H NMR displayed the characteristic $^{14}NH_4^+$ triplet (^JN-H = 52 Hz), whereas experiments under $^{15}N_2$ showed two doublets at 6.9 ppm (^JN-H = 73 Hz), confirming the formation of $^{15}NH_4^+$ (Figure 3c). For all tested single-ligand MOFs, no other reaction products were detected, confirming the selectivity of N_2-to-NH_3 conversion (Figures S18–S20). Interestingly, the observed activity trend does not correlate with the MOFs' optical absorption or electron-withdrawing strength. Although NO_2-MIL-101(Fe) exhibits the largest bandgap modulation, it does not show the highest catalytic activity. In contrast, Br-, F-, and CF_3-MIL-101(Fe) display only minor changes in their optical properties yet outperform NO_2-MIL-101(Fe) in NH_4^+ production.

Structure–Activity Relationship

The electronic impact of EWGs on the Fe centers was examined via Fe 2p XPS analysis. Relative to unmodified MIL-101(Fe), the Fe $2p_{3/2}$ binding energies shift positively by 0.3 eV (Br), 0.3 eV (F), 0.4 eV (NO_2), and 0.6 eV for CF_3-MIL-101(Fe), reflecting reduced electron density at Fe and a more ionic Fe-ligand bond. These shifts align with FTIR evidence of coordination modulation, showing that electron-withdrawing ligands deplete electron density at Fe, with the strongest effect observed for CF_3 substitution.

By contrast, the electron-donating NH_2 group does not induce a measurable shift (Figure S7, panels b-e). The impact of this modified Fe electron density on N_2 adsorption was further examined via temperature-programmed desorption (N_2-TPD) coupled with mass spectrometry (MS) to identify the desorption signals. Prior to measurements, samples were activated, saturated with N_2, and purged with He to remove excess N_2, including physisorbed molecules (details in the Methods). As shown in Figure S23, pristine MIL-101(Fe) and NH_2-MIL-101(Fe) exhibit desorption peaks at ∼ 150–60 °C, whereas samples functionalized with EWGs show higher desorption temperatures of ∼ 180 °C, ∼ 194 °C for CF_3-MIL-101(Fe), reaching 205 °C for NO_2-MIL-101(Fe).

Although several reports have attributed the high-temperature desorption peak (∼ 220 °C) to chemisorbed N_2,[43,44] our MS analysis (m/z = 44) shows that the signal instead corresponds to CO_2 desorption. This may originate from ligand decarboxylation or from removal of strongly chemisorbed CO_2. This CO_2 peak is distinct in the amino-functionalized sample, consistent with the reported high chemisorption due to hydrogen bonding between the oxygen electron pair in CO_2 and the hydrogen atoms of the NH_2 group.[45,46] In contrast, Br-, F-, NO_2-, and pristine MIL-101(Fe) exhibit CO_2 signals that partially overlap with the N_2 chemisorption peak. Nevertheless, PXRD and FTIR (Figure S21) reveal only minor differences before and after TPD, indicating that ligand decomposition contributes negligibly to the CO_2 signal. The N_2 uptake capacities are comparable among the samples, with values of 0.27 mmol g^{-1} for CF_3-MIL-101(Fe), 0.28 mmol g^{-1} for Br-MIL-101(Fe), 0.29 mmol g^{-1} for F-MIL-101(Fe) (Figure 4d), 0.34 mmol g^{-1} for pristine MIL-101(Fe), and 0.36 mmol g^{-1} for NO_2-MIL-101(Fe). For

https://doi.org/10.1021/jacs.5c22833
J. Am. Chem. Soc. 2026, 148, 21382–21392

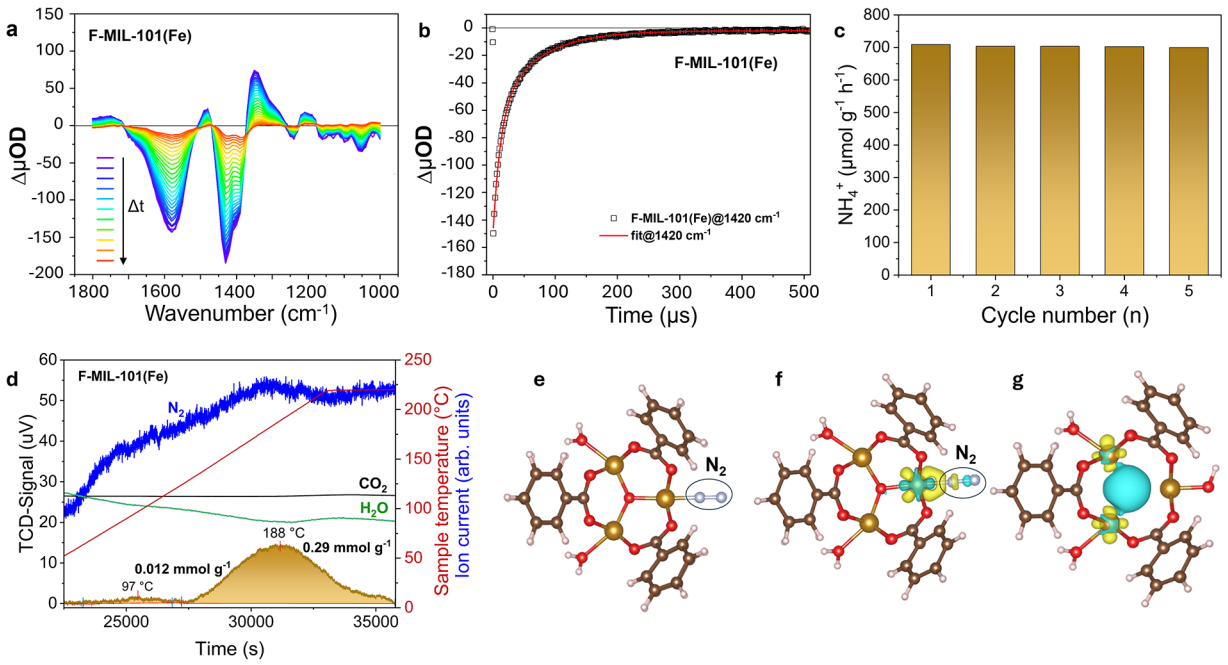

Figure 4. (a) TRIR difference absorption spectra of F-MIL-101(Fe) at varied time delays (140 ns−114 μs) upon 532 nm excitation. Spectra are color-coded from purple (early) to yellow (late), illustrating temporal evolution. (b) Corresponding decay kinetics with biexponential fits; at 1420 cm^{-1} the photoexcited F-MIL-101(Fe) exhibits biexponential decay with time constants of 11.8 ± 0.2 μs and 64.3 ± 0.9 μs. (c) NH_4^+ yield obtained from photocatalytic cycling experiments over F-MIL-101(Fe). (d) N_2-TPD-MS profile of F-MIL-101(Fe), showing chemisorbed N_2 desorption features. (e) DFT analysis on a cluster model of the MIL-101(Fe) SBU: end-on N_2 adsorption at an exposed Fe site. (f) Charge-density difference map illustrating N≡N bond polarization upon adsorption (cyan: charge depletion; yellow: charge accumulation). (g) Charge-density difference map showing electron distribution after removal of the μ_3-O atom.

Br-, F- and CF_3-MIL-101(Fe), this correlates with their specific surface areas, while NO_2-MIL-101(Fe) shows a notably higher uptake despite its lower surface area due to the bulky substituent. Importantly, the higher desorption temperatures of EWG-functionalized samples indicate stronger N_2 binding, consistent with FTIR evidence and the electron-withdrawing effects observed in XPS. Noteworthy differences are observed in the desorption peak shapes. NO_2-MIL-101(Fe) shows a very broad peak, reflecting both the moderate steric bulk of the NO_2 group (van der Waals radius 200−210 pm)[47] and stronger interactions between N_2 molecules and the framework during desorption, likely due to the polar and electron-withdrawing character of NO_2. In contrast, CF_3-MIL-101(Fe), despite being bulkier (van der Waals radius ∼ 220 pm),[47] exhibits a narrower peak, consistent with weaker interactions of N_2 with the CF_3 group, which is more hydrophobic and oriented away from the pore cavity. Br-MIL-101(Fe) (185 pm), F-MIL-101(Fe) (147 pm), and unfunctionalized MIL-101(Fe) show quite similar, moderately broad peaks, indicating intermediate interactions. These observations suggest that desorption behavior is influenced by steric hindrance imposed by the functional groups, emphasizing the importance of considering pore structure and dangling functional groups pointing inside the pore channels. On the other hand, MIL-88B(Fe) and F-MIL-88B(Fe) exhibit very low N_2 adsorption capacity (∼ 0.014−0.017 mmol g^{-1}, Figure S23g,h) due to closed pores and structural collapse under measurement conditions, as evident in postmeasurement PXRD patterns (Figure S24c), However, this does not reflect their behavior in aqueous photocatalysis, where the frameworks adopt an open-pore configuration allowing full reactant accessibility.[48] Accordingly, their photocatalytic NH_3 production reaches 114 and 191 μmol g^{-1} for MIL-88B(Fe) and F-MIL-88B(Fe), respectively (Figure S27b). No side products or N_2H_4 intermediates were detected for either sample (Figures S18−S20; Table S4).

Essentially, ligand functionalization tunes both the coordination strength and the electron density on Fe, both of which are critical for enabling N_2 activation. In NO_2-MIL-101(Fe), despite the electron-withdrawing properties of the NO_2 group that reduces electron density on Fe (as observed in XPS), the photocatalytic activity is similar to that of unfunctionalized MIL-101(Fe). This behavior likely arises from the strong electronegativity of the NO_2 group, which withdraws electron density from the coordinating oxygen atoms and serves as a sink for photogenerated holes, which is likely stabilized via resonance delocalization through the NO_2 aromatic π system. Similar to NH_2-MIL-101(Fe), this effect is supported by linear sweep voltammetry (LSV), which shows a higher water oxidation onset potential for NO_2-MIL-101(Fe) compared to unfunctionalized MIL-101(Fe) (Figure S21). Transient photocurrent measurements under chopped light further confirm slower hole extraction, with NO_2-MIL-101(Fe) exhibiting lower overall photocurrents than the other materials (Figure S22).

In contrast, other EWGs MOFs, such as Br-, F-, and CF_3-MIL-101(Fe), display opposite trends in LSV and photocurrent measurements, with lower onset potentials and higher photocurrents even compared to unfunctionalized MIL-101(Fe). These observations indicate that these variants achieve more efficient hole extraction and, correspondingly, higher photocatalytic performance, highlighting the importance of charge extraction.

https://doi.org/10.1021/jacs.5c22833
J. Am. Chem. Soc. 2026, 148, 21382−21392

While the bulk reaction medium is acidic (pH ∼ 3, Table S4), providing abundant protons, local surface charge effects modulate their accessibility at the Fe centers. The markedly lower ζ-potential of NO_2-MIL-101(Fe) (+6 mV vs +27 mV for MIL-101(Fe), Table S5) indicates an altered particle surface charge, which likely reduces the local availability of protons near the catalytic sites compared to the unfunctionalized MOF. In contrast, the slightly higher ζ-potential of NH_2-MIL-101(Fe) (28 mV vs 27 mV) suggests that protonation occurs at mainly the amino groups of the ligand, rather than at the Fe centers, illustrating how surface functionality can modulate proton distribution. Combined with its intrinsically poor N_2 chemisorption capacity and hole trapping, this renders NH_2-MIL-101(Fe) the least active sample for NH_4^+ formation. In contrast, halogenated ligands exhibit the opposite behavior. Although the bulk pH remains constant (pH ∼ 3), the surface ζ-potentials of Br-, F-, and CF_3-MIL-101(Fe) (+17, + 19, and +19 mV, respectively) are higher than that of NO_2-MIL-101(Fe) (+6 mV), suggesting enhanced retention of surface protons. Therefore, the electronegative halogen atoms repel protons away from the ligand, directing them toward the Fe centers. This explains why CF_3-MIL-101(Fe) and F-MIL-101(Fe) exhibit similar activity trends, despite the CF_3 variant having a lower surface area, and why the effect is slightly weaker for Br-MIL-101(Fe), consistent with the observed trend: F-MIL-101(Fe) > CF_3-MIL-101(Fe) > Br-MIL-101(Fe).

Protonation effects were further evaluated through pH-dependent activity tests. Upon increasing the initial pH of the dispersion to 7, both F-MIL-101(Fe) and NO_2-MIL-101(Fe) exhibit a clear decrease in activity, retaining approximately 60% and 70% of their initial NH_4^+ yields, respectively. At pH 8, the activity drops further to ∼ 25% and ∼ 20% of the initial values, and at pH 10 only a baseline activity of ∼ 14 μmol g^{-1} h^{-1} is observed for both materials (Figure S25a and b). This gradual decline reflects the reduced availability of H^+, which limits proton-coupled electron transfer steps essential for ammonia formation. In contrast, NH_2-MIL-101(Fe) exhibits a slight increase in activity at pH 7 compared to native dispersion pH of ∼ 3. This behavior can be attributed to partial deprotonation of surface $-NH_3^+$ groups, which reduces proton trapping and improves access to active sites. At higher pH (pH 8), the activity decreases again, indicating a transition to a regime where limited H^+ availability becomes the dominant factor. This is consistent with the trends observed for F- and NO_2-functionalized samples, which do not undergo significant functional group protonation and therefore show a continuous decline in activity with increasing pH.

Interactions between the carboxylate and the functional groups in the ligand tune the electronic environment of the SBU, impacting the lifetimes of the photoexcited states. In fact, reversible changes in coordination configuration can transiently expose delocalized Fe centers. This phenomenon, known as photoinduced dynamic ligation (PDL), was first reported in MIL-101(Fe)[21] and later observed in its NH_2- and NO_2-functionalized derivatives.[49] In this study, TRIR measurements further explored the occurrence of PDL in F-MIL-101(Fe) and Br-MIL-101(Fe). Specifically, the presence of excited state absorption (ESA) features at the far red and blue side of the measured spectral range (peaks around 1200 and 1750 cm^{-1}) reflected the formation of C−O and C = O bonds in the excited states (Figure 4a-b and Figure S26), indicating a transition from a symmetric ground state coordination to an asymmetric monodentate configuration upon photoexcitation, accompanied by the transient generation of delocalized Fe^{2+} states. Moreover, both F-MIL-101(Fe) and Br-MIL-101(Fe) exhibited two-component decay behavior (11.8 ± 0.2; 64.3 ± 0.9 μs and 12.0 ± 0.3; 62.6 ± 1.0 μs, respectively), similar to that observed in the NH_2-MIL-101(Fe) and NO_2-MIL-101(Fe) systems. According to a previous report,[49] the longer-lived component corresponds to excited states associated with the functional groups, indicating repulsive interactions between the negatively charged halogen and nearby oxygen atoms of the carboxylate group. The weighted average lifetimes of the photoexcited MOFs decreased in the order NO_2-MIL-101(Fe) > F-MIL-101(Fe) > Br-MIL-101(Fe) > MIL-101(Fe) > NH_2-MIL-101(Fe) (Table S7). This trend is partially consistent with the observed NH_4^+ production, with NO_2-MIL-101(Fe) as an exception, highlighting that catalytic performance is determined by multiple factors. Efficient N_2 hydrogenation relies on the interplay between charge-carrier dynamics and local proton availability, emphasizing that prolonged excited-state lifetimes alone are insufficient to achieve optimal activity.

To investigate how the redox cycle is sustained within the oxo-bridged trinuclear SBU, we tested a μ-oxo-centered trinuclear carboxylate complex, as a molecular analogue of the MIL-101(Fe) SBU. Its NH_4^+ synthesis performance was evaluated under identical conditions, with Fe molarity matched. The molecular complex produced 126 μmol g^{-1} h^{-1} of NH_4^+ (Figure S27a), nearly half of that observed with MIL-101(Fe), likely due to its lower structural stability. While the molecular complex loses crystallinity after reaction (Figure S35c), MIL-101(Fe) retains its crystalline framework, with initial activity observed even within the first 5 min and higher conversion rates over 1 h (Figures S28−S29). This underscores the advantage of the heterogeneous MOF approach in stabilizing the oxo-bridged SBU and sustaining NH_4^+ formation.

DFT calculations were performed to elucidate the N_2 activation mechanism. Adsorption energy calculations indicate that N_2 binds end-on at exposed Fe sites (Figure 4e, and Figures S31−32), polarizing the N≡N bond (Figure 4f). This is reflected in the PDOS, where the N_2 1π orbital shifts toward the Fermi level, accompanied by changes in the bonding 2σ orbital (Figure S33). These PDOS changes align with established N_2 activation mechanisms, where σ-donation from N_2 to Fe and π-backdonation from Fe d-orbitals to N_2 π^* orbitals facilitate activation.[50,51] While this explains N_2 activation on exposed Fe sites, the unique catalytic motif capable of performing both water oxidation and N_2 reduction remains elusive. Achieving a balance between electron acceptance and donation at a single active site is a known challenge for monometallic catalysts, as it involves a trade-off between these interactions.[52,53]

Observing the MIL-101(Fe) SBU structure and the fact that the molecular complex is also active, albeit with reduced stability, we propose that the central oxygen is crucial for catalytic function. The Fe^{3+} centers within the SBU behave as hard Lewis acid,[54] accepting electron density from N_2, consistent with the N_2 chemisorption observed under dark conditions in N_2-TPD experiments as the initial step of N_2 activation. The bridging μ_3-O atom withdraws electron density from the Fe centers, increasing their positive character and enhancing N_2 polarization. This is supported by Bader charge analysis of MIL-101(Fe) and the central-oxygen-removed

https://doi.org/10.1021/jacs.5c22833
J. Am. Chem. Soc. 2026, 148, 21382−21392

MIL-101(Fe), which indicates that removal of the μ_3-O atom leads to an increase in electronic charge on the nearby Fe centers (see Table S9 for Bader charge data), consistent with the charge redistribution (Figure 4g), resulting in unfavorable N_2 adsorption. DFT calculations further corroborate this behavior, showing that N_2 adsorption is highly endergonic (+2.05 eV) in the absence of the central oxygen but becomes favorable (−0.05 eV) when the μ_3-O is present. The PDOS shown in Figure S26 indicates that Fe initiates and dominates the unoccupied states, making it the most likely site to accept the photogenerated electrons. Upon illumination, the Fe centers adopt a delocalized Fe^{2+} character, enabling electron donation to the adsorbed N_2. Following electron transfer, the Fe^{2+} states revert to Fe^{3+}, with the central μ_3-O likely stabilizing the transient Fe^{2+} configuration.

Stability and Recyclability

Given that long-term performance is as important as initial activity, catalyst stability was evaluated. The structural integrity of the MOFs after catalysis was confirmed by PXRD (Figure S35). Inductively coupled plasma analysis of the reaction supernatant revealed only minor Fe leaching (Table S8). SEM images before and after catalysis showed no change in morphology, indicating good stability of the catalysts (Figure S36). In contrast, the molecular analogue released significantly higher Fe content under identical conditions, consistent with the loss of crystallinity observed in the postcatalysis PXRD pattern of the complex (Figure S35c). In addition, XPS spectra recorded before and after photocatalysis revealed only slight shifts of the Fe 2p binding energies, for all samples (Figures S6 and S7). Importantly, no change in oxidation state was observed, confirming the electronic stability of the framework under reaction conditions.

F-MIL-101(Fe) demonstrated the highest photocatalytic performance and retained its activity for up to five consecutive cycles (Figure 4c). Regarding their hydrophilicity, all MOF samples showed complete wetting (0° contact angle, Figure S37), due to strong capillary forces of porous materials. Furthermore, dynamic vapor sorption (DVS) measurements revealed a similar water uptake capacity of MIL-101(Fe), NH_2-MIL101(Fe), and F-MIL-101(Fe) (Figure S38). Due to the strong binding of water to the SBU a large hysteresis is observed. Collectively, the characterization of MIL-101(Fe) and its monofunctionalized derivatives, alongside photocatalytic testing and mechanistic studies, reveals how ligand chemistry modulates the properties and performance of this specific framework. Similar trends in photocatalytic activity were observed, confirming that the conclusions drawn for MIL-101(Fe) are not strictly system-specific. The observed behavior therefore supports that the same underlying principle - namely the role of proton availability - remains critical for both frameworks. We envision that this strategy could be extended to other photocatalytic systems, providing a versatile approach for rationally tuning photocatalytic performance in functional materials.

CONCLUSIONS

We synthesized a series of functionalized, photoactive MIL-101(Fe) MOFs to probe how ligand chemistry governs photocatalytic N_2-to-NH_3 conversion. In this system, the μ_3-oxo-centered trinuclear Fe cluster facilitates redox cycling through delocalized Fe^{2+} photoexcited states, which drive N_2 activation and stepwise protonation. By systematically varying the ligand, we disentangled electronic effects on Fe electron density, from protonation dynamics governed by active-site accessibility and functional group charge. Ligand substitution was correlated with N_2 binding and proton availability using complementary spectroscopic techniques (XPS, FTIR) and surface characterization methods (N_2-TPD, zeta potential), while TRIR spectroscopy revealed that ligand chemistry also controls the lifetimes of photoinduced charge-separated states following partial ligand dissociation at the Fe-oxo cluster.

Among the tested variants, fluorinated MIL-101(Fe) emerges as the benchmark, combining strong N_2 activation, favorable proton transfer kinetics, long-lived redox states, and high recyclability. In contrast, NH_2-functionalization reduces N_2 chemisorption, while also acting as a hole trap that localizes charge at the nitrogen atom and limits proton availability, thereby being detrimental to photocatalytic activity (Figure 5).

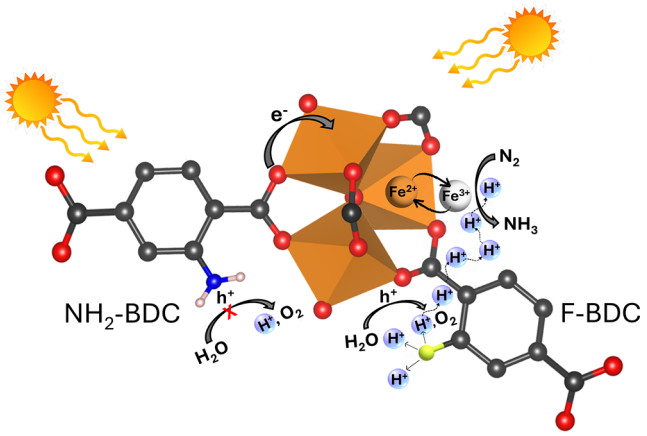

Figure 5. Schematic illustration of rate-determining steps in the MIL-101(Fe) SBU with NH_2-BDC and F-BDC ligands, showing hole trapping at the N atom of NH_2BDC versus favorable proton delivery toward Fe centers with F-BDC.

Similarly, NO_2-functionalization, despite enhancing N_2 chemisorption, withdraws electron density and localizes photogenerated holes, limiting proton availability and overall catalytic turnover.

ASSOCIATED CONTENT

Supporting Information

The Supporting Information is available free of charge at https://pubs.acs.org/doi/10.1021/jacs.5c22833.

Material synthesis; additional structural and spectroscopic characterization; details of photocatalytic experiments and detection; DFT calculation details; optimized geometries; atomic coordinates; data regarding catalyst stability (PDF)

AUTHOR INFORMATION

Corresponding Authors

Dominik Eder − *Institute of Materials Chemistry, TU Wien, 1060 Vienna, Austria;* orcid.org/0000-0002-5395-564X; Email: dominik.eder@tuwien.ac.at

Cornelia von Baeckmann − *Institute of Materials Chemistry, TU Wien, 1060 Vienna, Austria;* Email: cornelia.baeckmann@tuwien.ac.at

Authors

Jana Bischoff − *Institute of Materials Chemistry, TU Wien, 1060 Vienna, Austria;* orcid.org/0009-0004-2996-6957

Shaghayegh Naghdi − *Institute of Materials Chemistry, TU Wien, 1060 Vienna, Austria;* orcid.org/0000-0001-7738-2607

Adrian Ertl − *Institute of Materials Chemistry, TU Wien, 1060 Vienna, Austria*

Vasily Vorobyev − *Inorganic and Energy Chemistry, Department of Chemistry, Virginia Tech, Blacksburg, Virginia 24060, United States*

Anastasiia Naryshkina − *Institute of Materials Chemistry and Research, Faculty of Chemistry, University of Vienna, Vienna 1090, Austria*

Lakhanlal − *Department of Materials Science and Engineering, Technion - Israel Institute of Technology, Haifa 3200003, Israel;* orcid.org/0000-0002-3582-3854

Hanspeter Kählig − *Department of Organic Chemistry, University of Vienna, 1090 Vienna, Austria*

Laura Kronlachner − *Institute of Chemical Technologies and Analytics, TU Wien, 1060 Vienna, Austria*

Robert T. Woodward − *Institute of Materials Chemistry and Research, Faculty of Chemistry, University of Vienna, Vienna 1090, Austria;* orcid.org/0000-0003-0834-5137

Freddy Kleitz − *Department of Functional Materials and Catalysis, University of Vienna, 1090 Vienna, Austria;* orcid.org/0000-0001-6769-4180

Andreas Limbeck − *Institute of Chemical Technologies and Analytics, TU Wien, 1060 Vienna, Austria;* orcid.org/0000-0001-5042-2445

Maytal Caspary Toroker − *Department of Materials Science and Engineering and The Nancy and Stephen Grand Technion Energy Program, Technion - Israel Institute of Technology, Haifa 3200003, Israel; Resnick Sustainability Center for catalysis, Technion − Israel Institute of Technology, Haifa 3200003, Israel;* orcid.org/0000-0003-1449-2977

Amanda J. Morris − *Inorganic and Energy Chemistry, Department of Chemistry, Virginia Tech, Blacksburg, Virginia 24060, United States;* orcid.org/0000-0002-3512-0366

Complete contact information is available at: https://pubs.acs.org/10.1021/jacs.5c22833

Author Contributions

All authors have given approval to the final version of the manuscript.

Funding

Austrian Science Fund - Cluster of Excellence MECS (10.55776/COE5), Nancy and Stephen Grand Technion Energy Program (GTEP), Department of Energy (DE-SC0012445).

Notes

The authors declare no competing financial interest.

■ ACKNOWLEDGMENTS

This research was funded in whole or in part by the Austrian Science Fund (FWF) [10.55776/COE5]. For open access purposes, the author has applied a CC BY public copyright license to any author accepted manuscript version arising from this submission. The authors acknowledge the facilities of the Technical University of Vienna for technical support, especially Werner Artner from the X-ray center as well as the Analytical Instrumentation Center (AIC) led by Annette Foelske. Thanks to Stephen Nagaraju Myakala from TU Wien for supporting this work by TGA measurements and Stephan Puchegger from the faculty center for nanostructure research (University of Vienna) for his support with the SEM images. The work of A. J. Morris was supported by the Department of Energy under Grant DE-SC0012445. M. C. Toroker thanks the Nancy and Stephen Grand Technion Energy Program (GTEP) for their support.

■ REFERENCES

(1) Erfani, N.; Baharudin, L.; Watson, M. Recent Advances and Intensifications in Haber-Bosch Ammonia Synthesis Process. *Chemical Engineering and Processing - Process Intensification* **2024**, *204*, 109962.

(2) Chang, F.; Gao, W.; Guo, J.; Chen, P. Emerging Materials and Methods toward Ammonia-Based Energy Storage and Conversion. *Adv. Mater.* **2021**, *33* (50), 2005721.

(3) Ghavam, S.; Vahdati, M.; Wilson, I. A. G.; Styring, P. Sustainable Ammonia Production Processes. *Front. Energy Res.* **2021**, *9*, 580808.

(4) Erisman, J. W.; Sutton, M. A.; Galloway, J.; Klimont, Z.; Winiwarter, W. How a Century of Ammonia Synthesis Changed the World. *Nature Geosci* **2008**, *1* (10), 636−639.

(5) Castillejos, E.; García-Bordejé, E. Innovative Approaches to Sustainable Ammonia Synthesis under Mild Conditions. *ChemCatChem.* **2024**, *16* (13), No. e202301603.

(6) Shen, H.; Yang, M.; Hao, L.; Wang, J.; Strunk, J.; Sun, Z. Photocatalytic Nitrogen Reduction to Ammonia: Insights into the Role of Defect Engineering in Photocatalysts. *Nano Res.* **2022**, *15* (4), 2773−2809.

(7) Jia, H.-P.; Quadrelli, E. A. Mechanistic Aspects of Dinitrogen Cleavage and Hydrogenation to Produce Ammonia in Catalysis and Organometallic Chemistry: Relevance of Metal Hydride Bonds and Dihydrogen. *Chem. Soc. Rev.* **2014**, *43* (2), 547−564.

(8) Sharma, S.; Singh, H. D.; Kangotra, V.; Yadava, K. Introduction: Metal Organic Framework. In *Metal Organic Framework (MOFs)*; Kumar, P., Kumar, N., Aneja, D. K., Eds.; Springer Nature Singapore: Singapore, 2024; pp 1−18.

(9) Shi, Y.; Liu, Y.; Li, Q.; Liu, H.; Yang, D.; Jiang, Z. Nitrogen-Doped Metal−Organic Frameworks for Boosting Photocatalytic Ammonia Synthesis. *Trans. Tianjin Univ.* **2025**, *31* (6), 567−578.

(10) Sun, Q.; Zhu, Y.; Zhong, X.; Jiang, M.; Fan, Y.; Yao, J. Tuning Photoactive MIL-68(In) by Functionalized Ligands for Boosting Visible-Light Nitrogen Fixation. *ACS Appl. Mater. Interfaces* **2022**, *14* (48), 53904−53915.

(11) Huang, H.; Wang, X.-S.; Philo, D.; Ichihara, F.; Song, H.; Li, Y.; Li, D.; Qiu, T.; Wang, S.; Ye, J. Toward Visible-Light-Assisted Photocatalytic Nitrogen Fixation: A Titanium Metal Organic Framework with Functionalized Ligands. *Applied Catalysis B: Environmental* **2020**, *267*, 118686.

(12) Tang, Y.; Liu, Z.; Jia, J.; Zeng, H.; Rui, Z. Accelerating Electron Transfer Dynamics for Efficient Nitrogen Photoreduction on Nitrogenase-Mimicking Metal-Organic Framework/Fe-Dispersed MXene. *Applied Catalysis B: Environment and Energy* **2024**, *358*, 124426.

(13) Xin, Y.; Wang, L. An Enzyme-Mimicking Inorganic Catalyst for Effective Nitrogen Photofixation. *Chem. Catalysis* **2021**, *1* (1), 22−24.

(14) Wang, X.; Fan, G.; Guo, S.; Gao, R.; Guo, Y.; Han, C.; Gao, Y.; Zhang, J.; Gu, X.; Wu, L. Regulated Dual Defects of Bridging Organic and Terminal Inorganic Ligands in Iron-based Metal-Organic Framework Nodes for Efficient Photocatalytic Ammonia Synthesis. *Angew. Chem. Int. Ed* **2024**, *63* (22), No. e202404258.

(15) Zhao, Z.; Yang, D.; Ren, H.; An, K.; Chen, Y.; Zhou, Z.; Wang, W.; Jiang, Z. Nitrogenase-Inspired Mixed-Valence MIL-53(FeII/FeIII) for Photocatalytic Nitrogen Fixation. *Chemical Engineering Journal* **2020**, *400*, 125929.

(16) Zhang, Z.; Liu, C.; Chen, Y.; Chen, Q.; Shi, Y.; Wang, Z.; Bi, J.; Yu, J. C.; Wu, L. Defect Modulation of MIL-68(Fe) MOFs by Cu Doping for Boosting Photocatalytic N2 Fixation. *J. Catal.* **2024**, *432*, 115436.
(17) Guo, L.; Li, F.; Liu, J.; Jia, Z.; Li, R.; Yu, Z.; Wang, Y.; Fan, C. Improved Visible Light Photocatalytic Nitrogen Fixation Activity Using a Fe II -Rich MIL-101(Fe): Breaking the Scaling Relationship by Photoinduced Fe II /Fe III Cycling. *Dalton Trans.* **2022**, *51* (34), 13085−13093.
(18) Zhang, Z.; Li, F.; Li, G.; Li, R.; Wang, Y.; Wang, Y.; Zhang, X.; Zhang, L.; Li, F.; Liu, J.; Fan, C. Cu-Doped MIL-101(Fe) with Enhanced Photocatalytic Nitrogen Fixation Performance. *J. Solid State Chem.* **2022**, *310*, 123041.
(19) Feng, H.; Xu, Q.; Lv, T.; Liu, H. Bimetallic NH2-MIL-101(Fe, Co) as Highly Efficient Photocatalyst for Nitrogen Fixation. *Applied Catalysis B: Environment and Energy* **2024**, *351*, 123949.
(20) Zhu, Y.; Dong, Q.; Sial, A.; Labidi, A.; Zhao, K.; Li, X.; Wang, J.; Wang, C. Mixed-Metal MIL-101(Fe/Cr) MOF Photocatalyst: Efficient Photocatalytic Nitrogen Fixation by Promoting Ligand-Metal Charge Transfer. *Applied Catalysis O: Open* **2025**, *200*, 207030.
(21) Ye, Q.; Cairnie, D. R.; Troya, D.; Kumar, N.; Yang, X.; Morris, A. J. Photoinduced Dynamic Ligation in Metal−Organic Frameworks. *J. Am. Chem. Soc.* **2024**, *146* (1), 101−105.
(22) Skobelev, I. Y.; Sorokin, A. B.; Kovalenko, K. A.; Fedin, V. P.; Kholdeeva, O. A. Solvent-Free Allylic Oxidation of Alkenes with O2 Mediated by Fe- and Cr-MIL-101. *J. Catal.* **2013**, *298*, 61−69.
(23) Grosvenor, A. P.; Kobe, B. A.; Biesinger, M. C.; McIntyre, N. S. Investigation of Multiplet Splitting of Fe 2p XPS Spectra and Bonding in Iron Compounds. *Surface & Interface Analysis* **2004**, *36* (12), 1564−1574.
(24) Gecgel, C.; Simsek, U. B.; Turabik, M.; Ozdemir, S. Synthesis of Titanium Doped Iron Based Metal−Organic Frameworks and Investigation of Their Biological Activities. *J. Inorg. Organomet Polym.* **2020**, *30* (3), 749−757.
(25) Yang, M.; Tang, J.; Ma, Q.; Zheng, N.; Tan, L. High Activity Fe-MIL-101 Solid Acid Catalyst for Acetalization of Aldehydes with Methanol and Enamination of β-Dicarbonyl Compounds. *J. Porous Mater.* **2015**, *22* (5), 1345−1350.
(26) Vuong, G.-T.; Pham, M.-H.; Do, T.-O. Direct Synthesis and Mechanism of the Formation of Mixed Metal Fe2Ni-MIL-88B. *CrystEngComm* **2013**, *15* (45), 9694.
(27) Pazhand, H.; Sabbagh Alvani, A. A.; Sameie, H.; Salimi, R.; Poelman, D. The Exact Morphology of Metal Organic Framework MIL-53(Fe) Influences Its Photocatalytic Performance. *ChemistrySelect* **2023**, *8* (8), No. e202204538.
(28) Vuong, G.-T.; Pham, M.-H.; Do, T.-O. Synthesis and Engineering Porosity of a Mixed Metal Fe2 Ni MIL-88B Metal−Organic Framework. *Dalton Trans.* **2013**, *42* (2), 550−557.
(29) Cao, W.; Jiang, Z.; Gai, C.; Barrón, V.; Torrent, J.; Zhong, Y.; Liu, Q. Re-Visiting the Quantification of Hematite by Diffuse Reflectance Spectroscopy. *Minerals* **2022**, *12* (7), 872.
(30) Tran, T. V.; Nguyen, V. H.; Nong, L. X.; Nguyen, H.-T. T.; Nguyen, D. T. C.; Nguyen, T. T.; Nguyen, H. T. T.; Nguyen, T. D. Hexagonal Fe-Based MIL-88B Nanocrystals with NH2 Functional Groups Accelerating Oxytetracycline Capture via Hydrogen Bonding. *Surfaces and Interfaces* **2020**, *20*, 100605.
(31) He, J.; Zhang, Y.; Zhang, X.; Huang, Y. Highly Efficient Fenton and Enzyme-Mimetic Activities of NH2-MIL-88B(Fe) Metal Organic Framework for Methylene Blue Degradation. *Sci. Rep* **2018**, *8* (1), 5159.
(32) Vitillo, J. G.; Lu, C. C.; Cramer, C. J.; Bhan, A.; Gagliardi, L. Influence of First and Second Coordination Environment on Structural Fe(II) Sites in MIL-101 for C−H Bond Activation in Methane. *ACS Catal.* **2021**, *11* (2), 579−589.
(33) Wu, X.-P.; Gagliardi, L.; Truhlar, D. G. Cerium Metal−Organic Framework for Photocatalysis. *J. Am. Chem. Soc.* **2018**, *140* (25), 7904−7912.
(34) McKinlay, A. C.; Eubank, J. F.; Wuttke, S.; Xiao, B.; Wheatley, P. S.; Bazin, P.; Lavalley, J.-C.; Daturi, M.; Vimont, A.; De Weireld, G.; Horcajada, P.; Serre, C.; Morris, R. E. Nitric Oxide Adsorption and Delivery in Flexible MIL-88(Fe) Metal−Organic Frameworks. *Chem. Mater.* **2013**, *25* (9), 1592−1599.
(35) Guo, M.; Li, H. The Hydrolyzed Mil-88B(Fe) With Improved Surface Area for High-Capacity Lithium Ion Battery. *Front. Energy Res.* **2021**, *9*, 781008.
(36) Liu, N.; Xu, J.; Zhai, Y.; Zhang, Z.; Dang, Y.; Cao, Y.; Li, Z.; Huang, W.; Zhang, X.; Tang, L. Structure−Activity Relationship in Periodate Activation by Fe−MOFs: Why MIL-101(Fe) Outperforms Other MIL-Series in Antibiotic Degradation. *Green Energy & Environment* **2026**, *11*, 578.
(37) Lei, Z.; Xue, Y.; Chen, W.; Li, L.; Qiu, W.; Zhang, Y.; Tang, L. The Influence of Carbon Nitride Nanosheets Doping on the Crystalline Formation of MIL-88B(Fe) and the Photocatalytic Activities. *Small* **2018**, *14* (35), 1802045.
(38) Dabundo, R.; Lehmann, M. F.; Treibergs, L.; Tobias, C. R.; Altabet, M. A.; Moisander, P. H.; Granger, J. The Contamination of Commercial 15N2 Gas Stocks with 15N−Labeled Nitrate and Ammonium and Consequences for Nitrogen Fixation Measurements. *PLoS One* **2014**, *9* (10), No. e110335.
(39) Zhang, Z.; Li, X.; Liu, B.; Zhao, Q.; Chen, G. Hexagonal Microspindle of NH 2 -MIL-101(Fe) Metal−Organic Frameworks with Visible-Light-Induced Photocatalytic Activity for the Degradation of Toluene. *RSC Adv.* **2016**, *6* (6), 4289−4295.
(40) Gecgel, C.; Simsek, U. B.; Gozmen, B.; Turabik, M. Comparison of MIL-101(Fe) and Amine-Functionalized MIL-101(Fe) as Photocatalysts for the Removal of Imidacloprid in Aqueous Solution. *J. Iran Chem Soc* **2019**, *16* (8), 1735−1748.
(41) Taha, A. A.; Huang, L.; Ramakrishna, S.; Liu, Y. MOF [NH2-MIL-101(Fe)] as a Powerful and Reusable Fenton-like Catalyst. *Journal of Water Process Engineering* **2020**, *33*, 101004.
(42) Wang, J.; Cherevan, A. S.; Hannecart, C.; Naghdi, S.; Nandan, S. P.; Gupta, T.; Eder, D. Ti-Based MOFs: New Insights on the Impact of Ligand Composition and Hole Scavengers on Stability, Charge Separation and Photocatalytic Hydrogen Evolution. *Applied Catalysis B: Environmental* **2021**, *283*, 119626.
(43) Li, G.; Li, F.; Liu, J.; Fan, C. Fe-Based MOFs for Photocatalytic N2 Reduction: Key Role of Transition Metal Iron in Nitrogen Activation. *J. Solid State Chem.* **2020**, *285*, 121245.
(44) Zhao, Z.; Ren, H.; Shi, Y.; Tan, J.; Xin, X.; Yang, D.; Jiang, Z. Active Site Engineering in Heterovalent Metal Organic Frameworks for Photocatalytic Ammonia Synthesis. *Chemical Engineering Journal* **2022**, *443*, 136559.
(45) Yang, F.; Ma, J.; Chen, L. Study of the CO2 Adsorption Performance of a Metal−Organic Frameworks: Applications in Air Conditioning. *ChemistrySelect* **2023**, *8* (20), No. e202203314.
(46) Mahdipoor, H. R.; Halladj, R.; Ganji Babakhani, E.; Amjad-Iranagh, S.; Sadeghzadeh Ahari, J. Adsorption of CO2, N2 and CH4 on a Fe-Based Metal Organic Framework, MIL-101(Fe)-NH2. *Colloids Surf., A* **2021**, *619*, 126554.
(47) Atkins, P. W.; De Paula, J. *Elements of Physical Chemistry*, 6th ed.; Oxford University Press: Oxford, 2013.
(48) Ma, M.; Bétard, A.; Weber, I.; Al-Hokbany, N. S.; Fischer, R. A.; Metzler-Nolte, N. Iron-Based Metal−Organic Frameworks MIL-88B and NH2 -MIL-88B: High Quality Microwave Synthesis and Solvent-Induced Lattice "Breathing.". *Cryst. Growth Des.* **2013**, *13* (6), 2286−2291.
(49) Ye, Q.; Herlinger, I. A.; Fredin, L. A.; Cairnie, D. R.; Yang, X.; Yan, M.; Morris, A. J. Tuning the Lifetimes of Photoinduced Deligation in a Metal−Organic Framework via Linker Functionalization. *J. Am. Chem. Soc.* **2025**, *147* (38), 34690−34696.
(50) Wang, S.; Li, B.; Li, L.; Tian, Z.; Zhang, Q.; Chen, L.; Zeng, X. C. Highly Efficient N 2 Fixation Catalysts: Transition-Metal Carbides M 2 C (MXenes). *Nanoscale* **2020**, *12* (2), 538−547.
(51) Deng, G.; Pan, S.; Wang, G.; Zhao, L.; Zhou, M.; Frenking, G. Side-On Bonded Beryllium Dinitrogen Complexes. *Angew. Chem. Int. Ed* **2020**, *59* (26), 10603−10609.
(52) Zhao, Z.; Ren, H.; Yang, D.; Han, Y.; Shi, J.; An, K.; Chen, Y.; Shi, Y.; Wang, W.; Tan, J.; Xin, X.; Zhang, Y.; Jiang, Z. Boosting

Nitrogen Activation via Bimetallic Organic Frameworks for Photocatalytic Ammonia Synthesis. *ACS Catal.* **2021**, *11* (15), 9986−9995.
(53) Rai, R. K.; Al Maksoud, W.; Morlanés, N.; Harb, M.; Ahmad, R.; Genovese, A.; Hedhili, M. N.; Cavallo, L.; Basset, J.-M. Iron−Cobalt-Based Materials: An Efficient Bimetallic Catalyst for Ammonia Synthesis at Low Temperatures. *ACS Catal.* **2022**, *12* (1), 587−599.
(54) Pearson, R. G. Hard and Soft Acids and Bases, HSAB, Part 1: Fundamental Principles. *J. Chem. Educ.* **1968**, *45* (9), 581.

https://doi.org/10.1021/jacs.5c22833
J. Am. Chem. Soc. 2026, 148, 21382−21392